Article

Structure

Structures of drug-specific monoclonal antibodies bound to opioids and nicotine reveal a common mode of binding

Graphical abstract

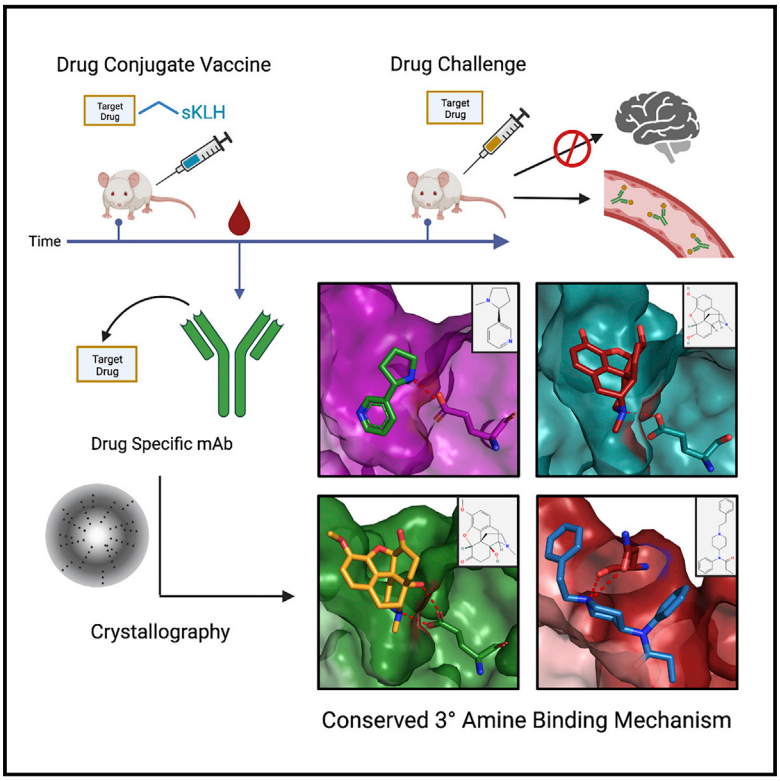

Highlights

- Structures of drug-conjugate vaccine-elicited mAbs bound to nicotine and opioids
- Structures of free-drug oxycodone and fentanyl bound to mAbs
- Conserved protonated amine opioid-drug binding mechanism
- Complementary pocket charge mechanism may be required for high-affinity binding

Authors

Justas V. Rodarte, Carly Baehr, Dustin Hicks, ..., Scott Runyon, Marco Pravetoni, Marie Pancera

Correspondence

mprave@uw.edu (M.P.), mpancera@fredhutch.org (M.P.)

In brief

Rodarte et al. report on the structural mechanisms underlying vaccine-elicited antibodies and monoclonal antibodies (mAbs) targeting commonly misused drugs such as the synthetic opioid fentanyl. Vaccines and mAbs are promising treatment avenues for addressing the rising opioid epidemic by targeting the drug directly.

Rodarte et al., 2023, Structure *31*, 20–32
January 5, 2023 © 2022 Elsevier Ltd.
https://doi.org/10.1016/j.str.2022.11.008

CellPress

CellPress

Structure

Article

Structures of drug-specific monoclonal antibodies bound to opioids and nicotine reveal a common mode of binding

Justas V. Rodarte,[1] Carly Baehr,[2] Dustin Hicks,[2] Tyler L. Liban,[1] Connor Weidle,[1] Peter B. Rupert,[3] Rajwana Jahan,[4] Abigail Wall,[1] Andrew T. McGuire,[1,5,6] Roland K. Strong,[3] Scott Runyon,[4] Marco Pravetoni,[2,7,8,*] and Marie Pancera[1,9,*]

[1]Vaccine and Infectious Disease Division, Fred Hutchinson Cancer Center, Seattle, WA, USA
[2]Department of Pharmacology, University of Minnesota Medical School, Minneapolis, MN, USA
[3]Basic Science Division, Fred Hutchinson Cancer Center, Seattle, WA, USA
[4]Research Triangle Institute International, Research Triangle Park, Durham, NC, USA
[5]Department of Global Health, University of Washington, Seattle, WA, USA
[6]Department of Laboratory Medicine and Pathology, University of Washington, Seattle, WA, USA
[7]Department of Psychiatry and Behavioral Sciences, Department of Pharmacology, School of Medicine, University of Washington, Seattle, WA, USA
[8]Center for Medication Development for Substance Use Disorders and Overdose, University of Washington, Seattle, WA, USA
[9]Lead contact
*Correspondence: mprave@uw.edu (M.P.), mpancera@fredhutch.org (M.P.)
https://doi.org/10.1016/j.str.2022.11.008

SUMMARY

Opioid-related fatal overdoses have reached epidemic proportions. Because existing treatments for opioid use disorders offer limited long-term protection, accelerating the development of newer approaches is critical. Monoclonal antibodies (mAbs) are an emerging treatment strategy that targets and sequesters selected opioids in the bloodstream, reducing drug distribution across the blood-brain barrier, thus preventing or reversing opioid toxicity. We previously identified a series of murine mAbs with high affinity and selectivity for oxycodone, morphine, fentanyl, and nicotine. To determine their binding mechanism, we used X-ray crystallography to solve the structures of mAbs bound to their respective targets, to 2.2 Å resolution or higher. Structural analysis showed a critical convergent hydrogen bonding mode that is dependent on a glutamic acid residue in the mAbs' heavy chain and a tertiary amine of the ligand. Characterizing drug-mAb complexes represents a significant step toward rational antibody engineering and future manufacturing activities to support clinical evaluation.

INTRODUCTION

Over the past two decades, annual fatal overdoses linked to opioids in the United States have rapidly increased, from fewer than 10,000 in 2000 to 49,860 in 2019. In 2020 that number spiked to 69,090, an increase of 38.6% over 2019.[1] Data from 2021 indicate an even steeper increase due to the additional multifactorial impact of the COVID-19 pandemic,[1] surpassing 100,000 deaths in the United States alone. Current pharmacotherapies and behavioral interventions against opioid use disorder (OUD) are suboptimal, and the COVID-19 pandemic has further complicated outreach and treatment.[2,3] More effective treatments are needed to help control the opioid epidemic, particularly ones that impose minimal burden on strained public health resources. To this end, immunotherapeutics such as anti-opioid vaccines and monoclonal antibodies (mAbs) would represent a significant advancement in therapeutics for OUD and overdose.[4]

In 2020 the National Institutes of Health reported that 2.7 million people in the United States are currently living with an OUD.[5] Worldwide ~40–80 million people use opioids, although the frequency of such use is not well defined.[6] In addition to outreach programs such as Narcotics Anonymous and behavioral treatments, several pharmacotherapeutic interventions exist for OUD, including opioid receptor agonists (methadone), partial agonists (buprenorphine), antagonists (naloxone and naltrexone), and agonist/antagonist combinations (e.g., Suboxone).[7] However, these treatments have significant limitations which have only been further complicated by the ongoing COVID-19 pandemic. Methadone regimens need daily dosing, requiring staff for observation and patient transport to the facility; staffing shortages have had negative impacts on these services.[8] Naloxone, while effective, often requires higher or multiple doses to treat overdoses from fentanyl, carfentanil, and their analogs.[9] For patients outside of treatment, access to and the use of illegal narcotics carries a risk of infection and health complications from blood-borne and airborne pathogens such as HIV, hepatitis C, and SARS-CoV-2.[10,11] While policy changes have the potential to abate some of the complications of existing

CellPress

treatments in light of the COVID-19 pandemic,[2,3,8] novel treatments for OUD were already considered a necessary innovation prior to 2019.[12,13]

Drug-conjugate vaccines and mAbs are promising treatments for OUD and may overcome some of the limitations of current pharmacotherapies. Conjugate vaccines consist of a drug-based hapten conjugated to an immunogenic carrier protein, which elicits a drug-specific polyclonal antibody response against a targeted drug. Antibodies, vaccine-elicited or ready-made, bind the target drug and prevent its distribution to the brain, reducing overall unbound drug concentrations. Unlike small-molecule therapies, antibody-based therapies are effective on a weeks-long (mAb) or months-long (vaccine) timescale.[14,15] Additionally, antibodies do not directly affect signaling at opioid receptors and carry fewer side effects. Perhaps most importantly, mAbs against highly potent synthetic opioids have the potential to negate or rescue from otherwise lethal doses of these drugs, providing both a preventive and therapeutic intervention to directly reduce opioid overdose deaths.[14,16] Drug-specific mAbs have been shown to reduce behavioral and pharmacological effects of opioids such as self-administration, respiratory depression, bradycardia, antinociception, and locomotor activity in mice, rats, and non-human primates.[14–16] Vaccines and/or mAbs could be administered to specific patient populations depending on the clinical scenario related to either treatment of OUD or rescue from overdose. Both approaches have been shown to not interfere with current pharmacotherapies.[16,17] The longevity of antibody-based treatments can reduce the treatment burden on healthcare facilities and the need for daily or weekly compliance by patients. It is also not possible to abuse, resell, or overdose on vaccines or mAbs, reducing regulatory burdens, risk of illegal diversion, and abuse liability associated with agonists such as methadone.

High-potency synthetic drugs such as fentanyl and carfentanil present favorable targets for mAb-based therapies, as drugs with larger effective doses can quickly saturate antibody titers. This limitation was a major obstacle to an effective nicotine vaccine,[18] as minimum effective titers could only bind the molar equivalent of one cigarette. However, effective mAb-based therapies against drugs of abuse have seen recent successes. An anti-cocaine mAb, h2E2, is in late-stage preclinical development,[19] and an anti-methamphetamine mAb, IXT-m200, has completed phase I and phase II clinical trials (NCT05034874), supporting the continued investigation of mAbs targeting small-molecule drugs. The OXY-KLH vaccine targeting oxycodone is currently in phase Ia/Ib clinical trials.[20] An overview of completed and ongoing clinical trials is reviewed elsewhere.[21] The potency and diversity of emerging synthetic opioids highlights the need for more effective counteragents[1] but also presents a more favorable molar ratio for sequestration by mAb compared with higher LD_{50} drugs such as nicotine. Considering current treatment limitations and the properties of these emerging synthetic drugs, mAb-based therapies show significant promise as additional treatments to help address the rising opioid epidemic.

Previously, we elicited the anti-drug mAbs NIC311, HY4-1F9, HY2-A12, and HY6-F9 through immunizing mice with a vaccine consisting of the target drug conjugated to the keyhole limpet hemocyanin subunit (drug-sKLH vaccine), or in the case of NIC311, conjugated to the *P. aeruginosa* exoprotein A carrier protein. In mice, passive immunization with these lead mAbs showed serum sequestration of the target drug, 50%–80% reduced drug concentration in the brain, and reduced behavioral and pharmacological effects.[20,22] Competitive ELISA revealed mAb *in vitro* relative binding affinities in the 0.5 nM to 1.5 μM range to their respective drug targets morphine, oxycodone, and fentanyl,[20] and 60 nM for the target nicotine.[22]

To date, no data regarding the specific binding mechanism of these drug-mAb complexes have been available. Here, we report the crystal structures of the aforementioned mAbs complexed with nicotine, oxycodone, morphine, and fentanyl, respectively. Kinetic affinity of mAbs for haptens derived from these drugs was assessed by biolayer interferometry (BLI), and the structures were compared with known mAbs and endogenous receptors that bind structurally similar ligands. By investigating these structures at near-atomic resolution, we were able to observe specific functional group coordination and identify key conserved features that determine mAb affinity for these drug targets. Characterizing the mode of antibody-drug binding will support ongoing humanization, manufacturing, and qualification of lead mAbs against fentanyl and its analogs being readied for clinical trials. By illuminating the mechanism of this molecular recognition, we hope to use rational design to develop more effective vaccines and mAbs against emerging synthetic opioids.

RESULTS

Structural characterization of NIC311 in complex with nicotine

NIC311 was isolated through immunization of mice with a nicotine-based hapten conjugated to recombinant *P. aeruginosa* exoprotein A carrier protein, in which the nicotine was attached to the carrier at the C-5 of the pyrrolidine ring (Figure S1).[22] We solved the structure of the NIC311 antigen-binding fragment (Fab) bound to nicotine to 2.2 Å, with one Fab in the unit cell (Table 1).

The nicotine molecule is oriented vertically in a five-sided pocket, formed primarily by aromatic residues (Figure 1A). Two additional residues, $Glu50_{HC}$ and $Asn34_{LC}$, following Kabat numbering,[24] contribute polar interactions and contact both nitrogen-containing functional groups on the nicotine ligand. Analysis using the software dr_sasa[25] indicates that the nicotine ligand has an accessible surface area of ~327 $Å^2$ and a buried surface area (BSA) of ~296 $Å^2$, ~180 $Å^2$ from the heavy chain (HC) and ~115 $Å^2$ from the light chain (LC) (Figure S2), indicating that the ligand is 90% enclosed within the binding site (Figure S2).

Nicotine forms ~152 $Å^2$ of contact with residues within the NIC311 binding pocket, described as the contact surface area (CSA) of the nicotine ligand to the Fab. This includes ~86 $Å^2$ of contact to the HC and ~66 $Å^2$ to the LC (Figure 1B). Nearly half of CDR3 residues in NIC311 are aromatic, although the ligand only contacts a few. The frequency of bulky side chains may preclude close packing of these aromatic residues due to steric repulsion, forming a more open binding site than seen in other structures (Figure 1A). This pocket shape likely allows nicotine-exoprotein A linker egress, which can be seen in Figures 1A

Table 1. Data collection and refinement statistics for crystal structures

	NIC311	HY4-1F9	HY2-A12	HY6-F9
Data collection				
Space group	C121	$P2_1$	P1	$P3_1$
Cell dimensions				
a, *b*, *c* (Å)	114.76, 71.33, 57.34	58.79, 97.18, 76.13	67.62, 67.99, 85.62	218.14, 218.14, 89.02
α, β, γ (°)	90, 107.66, 90	90, 91.23, 90	69.13, 67.60, 68.64	90, 90, 120
Resolution (Å)	50.00–2.10 (2.18–2.10)	50.00–1.81 (1.84–1.81)	50.00–2.24 (2.28–2.24)	50.00–1.75 (1.78–1.75)
R_{merge} [a]	0.052 (0.5604)	0.072 (0.332)	0.051 (0.542)	0.155 (0.998)
$\langle I/\sigma(I)\rangle$	22.52 (1.20)	18.48 (4.11)	20.73 (1.80)	7.7 (1.3)
$CC_{1/2}$	0.992 (0.667)	0.986 (0.902)	0.995 (0.716)	0.994 (0.989)
Completeness	99.5 (96.8)	98.47 (87.8)	89.12 (61.1)	99.6 (98.9)
Redundancy	1.8 (1.7)	3.5 (3.1)	1.8 (1.6)	5.1 (5.0)
Refinement				
Resolution (Å)	50.00–2.10 (2.18–2.10)	47.01–1.82 (1.89–1.82)	42.85–2.3 (2.38–2.30)	43.3–1.75 (1.81–1.75)
No. of unique reflections	25,737 (2,512)	75,630 (7,370)	52,370 (3,647)	475,987 (47,293)
R_{work} [b]/R_{free} [c]	23.3/26.3 (33.5/34.1)	17.0/20.8 (20.4/24.1)	22.1/28.0 (26.8/34.1)	19.7/22.6 (27.2/30.5)
No. of atoms	3,303	7,096	9,612	33,436
Protein	3,187	6,610	9,304	30,132
Water	89	329	711	2,829
Ligand	27	157	132	475
B factors (Å^2)	43.32	19.98	36.71	23.94
Protein	43.24	19.52	36.91	23.20
Water	41.05	25.82	30.45	31.19
Ligand	60.32	28.28	36.91	28.12
RMS bond length (Å)	0.007	0.008	0.004	0.006
RMS bond angle (°)	0.90	1.07	0.75	0.90
Ramachandran plot statistics [d]				
Residues	425	867	1,258	3,942
Most favored region	95.70	97.08	97.25	97.24
Allowed region	3.82	2.92	2.67	2.76
Disallowed region	0.48	0.00	0.08	0.0
Clashscore	8.14	3.26	2.32	3.48
PDB ID	7U61	7U62	7U63	7U64

[a] $R_{merge} = [\sum_h\sum_i|I_h - I_{hi}|/\sum_h\sum_i I_{hi}]$, where I_h is the mean of I_{hi} observations of reflection *h*. Numbers in parentheses represent highest-resolution shell.
[b] R_{factor} and
[c] $R_{free} = \sum||F_{obs}| - |F_{calc}||/\sum|F_{obs}| \times 100$ for 95% of recorded data (R_{factor}) or 5% data (R_{free}).
[d] Calculated using MolProbity.[23]

and S1. Since nicotine is highly symmetrical, we could not definitely determine its orientation at 2.2 Å resolution. We used the C-5 linker conjugation point to orient the molecule, where a channel adjacent to C-5 could be seen to accommodate this linker (Figure 1). F_O-F_C map analysis upon orientation changes further confirmed our selected nicotine orientation.

The interaction of $Glu50_{HC}$ is dependent on protonation of nicotine to form a 2.5 Å hydrogen bond, serving as a strong binding interaction and anchoring NIC311 in the pocket. Additionally, this protonation forms the cation for a π-cation interaction with $Trp33_{HC}$. The pyrrolidine and pyridine nitrogens have a pK_a of 8.01 and 3.1, respectively.[26] Hence, at our crystallographic pH of 5.5 (Table 2), and likely under physiological pH, the pyrrolidine nitrogen is protonated. At pH 7.4, NIC311 has an affinity of 2.4 nM for the 3AmNic-biotin hapten (Table 3). Further BLI runs conducted in PBS-T buffer at ~0.5 pH increments, from pH 5 to 10, showed a reduction in BLI signal in buffers with pH above 7.4 and below 7.0, but apparently no significant change to calculated K_D (Table 4 and Figure S4).

The structure of another nicotine-binding Fab, NIC12, has previously been published (PDB: 2YK1).[27] To understand their differences in binding, we compared the structures by superimposing the Fv domains (1.08 Å root-mean-square deviation [RMSD] over 178 Cα atoms).[28] Additionally, NIC12 has a reported K_D of ~7.4 nM as determined by equilibrium dialysis,[29] while NIC311 has a K_D of ~2.4 nM as determined by BLI (Table 2) and ~60 nM as determined by competitive ELISA.[22] The binding pocket of NIC12 is far deeper and more enclosed than NIC311 (Figure 1C), requiring complementarity-determining region (CDR) loop movement for nicotine to enter or exit the pocket.[27]

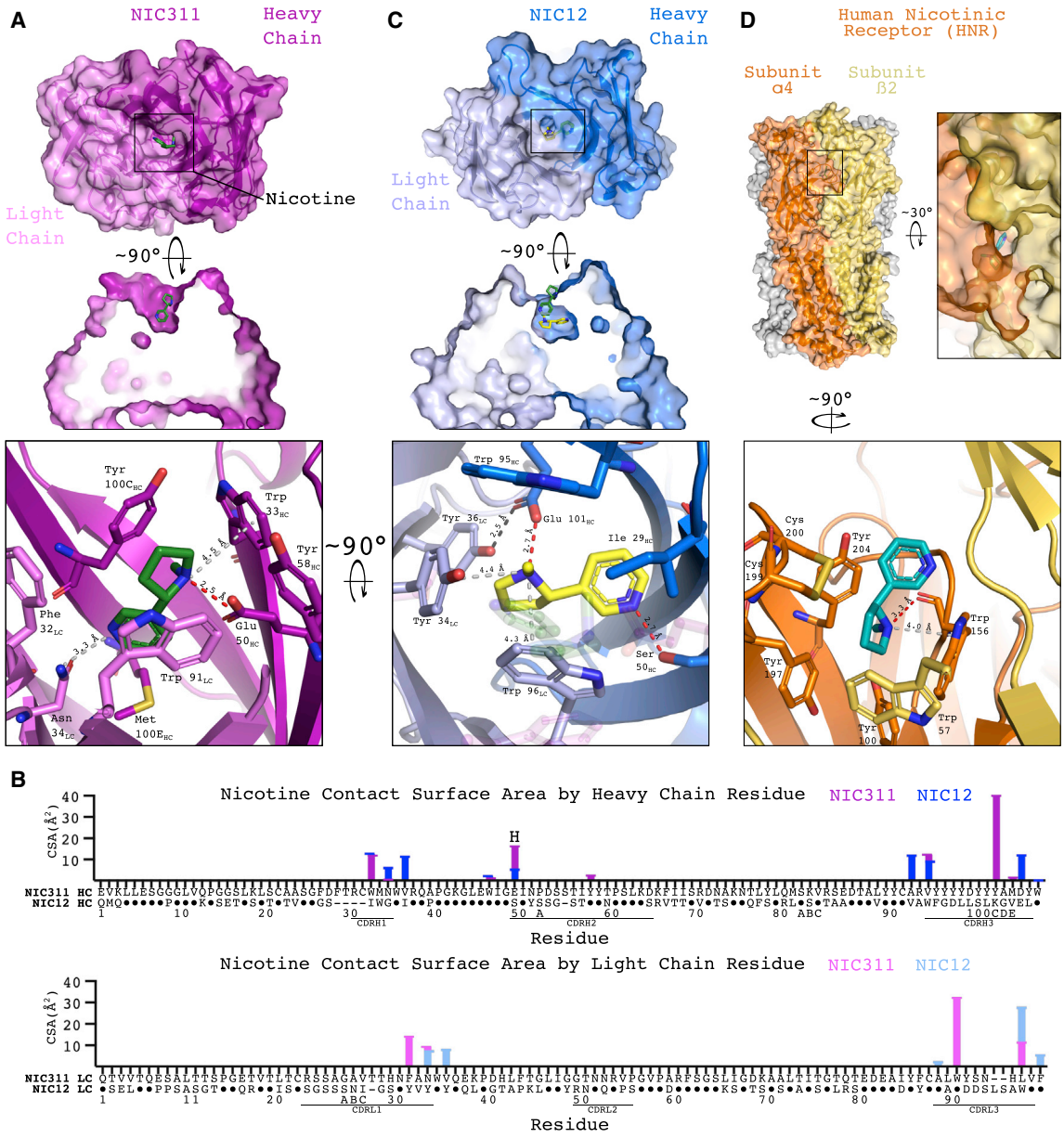

Figure 1. Structures of NIC311 Fab in complex with nicotine, compared with NIC12 Fab and the human nicotinic receptor bound to nicotine

(A) Top: surface representation of NIC311 Fab with nicotine, shown as green sticks, in the binding pocket of NIC311 in two orientations. Bottom: the binding site is shown in detail with key residues shown as sticks. Red bonds correspond to hydrogen bonds and light-gray bonds to van der Waals interactions.

(B) CSA plot of the nicotine ligand and NIC311 or NIC12 residues, with a sequence alignment of NIC311 and NIC12 shown below. Residues involved in hydrogen bonding are marked with an "H." Bar data are superimposed. Dots indicate conserved residues, dashes indicate gaps in the aligned sequences, and numbering and CDRs are true to NIC311.

(C) Top: nicotine, depicted as yellow sticks, is shown in the NIC12 binding pocket, and compared with the relative position of nicotine in the NIC311 pocket (green). Bottom: the NIC12 binding site is shown similarly to Figure 1A, with the NIC311 site superimposed. Black bonds correspond to intra-Fab hydrogen bonds or salt bridges.

(D) The human nicotinic receptor is shown with the α4 and β2 subunits colored as indicated, with nicotine shown as teal sticks. An in-depth binding site is shown on the right.

Despite a greater BSA, nicotine forms about 20% (~32 Å^2) less contact (CSA) with NIC12 than with NIC311 (Figures S2 and S3). In both structures, the hydrogen bond to the ligand is formed by a glutamic acid residue (Glu101$_{HC,NIC12}$). Additionally, two π-cation interactions form in NIC12, Tyr34$_{LC,NIC12}$ and Trp96$_{LC,NIC12}$, while a single π-cation interaction forms in NIC311 (Figure 1C). While the residues in these interactions are structurally similar, they are not conserved (Figure 1B). One notable difference is that NIC12 forms an additional hydrogen bond between the pyridine ring and Ser50$_{HC,NIC12}$, a bond that

Table 2. Crystallization conditions

mAb	Ligand	mAb concentration (mg/mL)	Well condition
NIC311	Nicotine	6.4	0.1 M MES pH 5.5, 15% PEG 4000, 90 mM ammonium sulfate
HY4-1F9	Morphine	12	20% PEG 8000, 0.1 M Na cacodylate, 0.2 M Mg acetate, 2.25% xylitol
HY2-A12	Oxycodone	5	0.1 M Tris pH 8.5, 20% PEG 3350, 20% isopropanol
HY6-F9	Fentanyl	20	2.8 M sodium acetate

PEG, polyethylene glycol.

is not formed in NIC311 with the structurally equivalent residue, $Asn34_{LC,NIC311}$, which likely provides a weaker electrostatic interaction. To create the more enclosed pocket of NIC12, $Trp95_{HC,NIC12}$ and $Ile29_{HC,NIC12}$ act as hydrophobic "caps" that appear to move into place above nicotine when bound, improving drug sequestration (Figure 1C).

While NIC311 and NIC12 show similarities despite different residue identities and pocket structure, we also sought to determine whether they share structural similarity to the human nicotinic receptor (HNR). We compared the key nicotine-binding residues of NIC311 with the $\alpha4/\beta2$ subunit interface of the HNR, the most common subunit interface type (PDB: 5KXI) (Figure 1D).[30] The only notable similarity between these is that the ligand is >90% buried; otherwise, the binding mechanisms are distinct. In the HNR, only one residue forms bonds, coordinating the ligand with Trp156 of the $\alpha4$ subunit (Figure 1D). The backbone amide forms a hydrogen bond with the protonated pyrrolidine amine, while the tryptophan pyrrole ring forms a π-cation interaction with the same amine. Beyond this singular residue interaction, the multiple interacting residues observed in NIC311 or NIC12 are absent. Despite these differences, the $\alpha4/\beta2$ subunit displays a similar affinity, with a published affinity range of 0.6–10 nM.[30] The HNR also binds a diverse repertoire of ligands, including nicotine and acetylcholine among other agonists and antagonists.

Structural characterization of HY4-1F9 in complex with morphine

The mAb HY4-1F9, targeting heroin, 6-acetylmorphine, and morphine, was isolated from mice immunized with a conjugate vaccine consisting of a morphine hapten attached at the C-6 alcohol, replacing the hydroxyl group with a ketoxime ether $(Gly)_4$ linker to sKLH (Figure S1).[20] MOR-sKLH has been shown to be effective against heroin and its metabolites.[4] Binding affinity measurements by BLI indicated that HY4-1F9 has an affinity of 120 ± 7 pM for the biotinylated morphine hapten (Table 3 and Figure S5). To further understand this high-affinity binding at the molecular level, we solved the structure of HY4-1F9 Fab bound to morphine to 1.8 Å, with two Fabs in the unit cell (Table 1).

Our structure reveals the binding pocket of HY4-1F9 to be a depression with a shallow overhang, under which the morphine ligand sits. This site is primarily constructed of aromatic residues, between which $Glu50_{HC}$ protrudes in toward the tertiary amine of morphine (Figure 2A). Morphine has a pK_a of 8.08[31]; the tertiary amine is likely protonated at our crystallization pH of 7.0 (Table 2) and at physiological pH, forming a strong 2.5 Å hydrogen bond with $Glu50_{HC}$. We sought to understand whether pH and protonation state of this amine played a key role in binding. However, a BLI binding assay of HY4-1F9 to the biotinylated hapten, conducted at pH 5.8, 7.4, and 10.0, in 2-(N-morpholino) ethanesulfonic acid (MES), PBS, and carbonate buffer, respectively, showed that while binding was not ablated, slightly higher K_D was observed at higher pH (Table 4). The tertiary amine also forms two π-cation interactions with residues in the base of the pocket, $Tyr100D_{HC}$ and $Trp91_{LC}$ (Figure 2A), for which tertiary amine protonation is required. These three interactions occur in a roughly trigonal geometry, anchoring the ligand to the base of the pocket. Additionally, the $Phe100A_{HC}$ backbone amide of the CDRH3 overhang forms a hydrogen bond with the C-3 phenolic hydroxyl group of morphine (Figure 2A). There is a >2-fold greater BSA from the HC than the LC in HY4-1F9 (~262 $Å^2$ versus ~103 $Å^2$, Figure S2), and a >3-fold greater CSA (~145 $Å^2$ versus ~45 $Å^2$). Aside from $Trp91_{LC}$, the ligand contacts only one other LC residue, $Tyr32_{LC}$, which forms a 90° π-π interaction with the aromatic ring.

One Fab crystal structure, mAb 9B1, has been solved previously with its morphine ligand (PDB: 1Q0Y), with a reported affinity of ~1 nM,[32] compared with HY4-1F9's affinity of 124 pM (Table 3). Following alignment of the FV domains of 9B1 and HY4-1F9 (0.944 Å RMSD over 205 Cα atoms),[28] we found that coordination of the protonated tertiary amine is nearly identical between HY4-1F9 and 9B1; the only difference is that $Trp95_{HC,9B1}$ substitutes for $Tyr100D_{HC,HY4\text{-}1F9}$. At a crystallization pH of 4.6, 9B1 forms a hydrogen bond of ~2.6 Å between $Glu50_{HC,9B1}$ and the protonated tertiary amine, along with two π-cation interactions in the same trigonal arrangement as HY4-1F9 (Figure 2B). Sequence comparison indicates that these antibodies share the same IGLV1*01 mouse germline gene but have different VH germline genes: HY4-1F9 uses IGHV4-1*02 while 9B1 uses IGHV9*01.[33] Nearly all key residues which the ligand contacts are conserved, except for residue 58_{HC} and residues in the CDRH3 (Figure 2D). Beyond the amine-binding motif, 9B1 shows no further ligand coordination. Pozharski et al.[32] also reported that an apo structure of 9B1 displayed only minor differences from the bound structure, consistent with small residue adjustments to form optimal bond geometry, suggesting a lock-and-key mechanism. Hence, the largest structural difference between the two is the longer CDRH3 loop of HY4-1F9, which increases ligand BSA but not CSA (Figures S2 and S3). An additional difference is the catemer of $Glu35_{HC,\ 9B1}$ and $Glu50_{HC,\ 9B1}$, a feature that is absent in HY4-1F9. Considering the similarities between these Fabs, the difference in affinity may be a result of one or both of these structural variations.

Table 3. BLI results of NIC311, HY2-A12, HY4-1F9, and HY6-F9

mAb	Ligand	K_D (M)	K_{on} (1/Ms)	K_{dis} (1/s)	Full R^2
NIC311	3AmNic-biotin	$(2.4 \pm 0.04) \times 10^{-9}$	$(6.6 \pm 0.1) \times 10^{5}$	$(1.6 \pm 0.01) \times 10^{-3}$	0.9508
HY2-A12	OXY-biotin	$(1.0 \pm 0.02) \times 10^{-9}$	$(2.8 \pm 0.02) \times 10^{5}$	$(2.7 \pm 0.05) \times 10^{-4}$	0.9982
HY4-1F9	OXY-biotin	$(1.2 \pm 0.02) \times 10^{-9}$	$(1.7 \pm 0.006) \times 10^{5}$	$(2.1 \pm 0.04) \times 10^{-4}$	0.9993
HY6-F9	OXY-biotin	NDB	NDB	NDB	NDB
HY2-A12	MOR-biotin	$(7.7 \pm 0.2) \times 10^{-9}$	$(2.8 \pm 0.02) \times 10^{5}$	$(2.7 \pm 0.05) \times 10^{-4}$	0.9461
HY4-1F9	MOR-biotin	$(1.2 \pm 0.07) \times 10^{-10}$	$(2.0 \pm 0.007) \times 10^{5}$	$(2.5 \pm 0.01) \times 10^{-5}$	0.9999
HY6-F9	MOR-biotin	NDB	NDB	NDB	NDB
HY2-A12	F-biotin	NDB	NDB	NDB	NDB
HY4-1F9	F-biotin	$(1.3 \pm 0.06) \times 10^{-9}$	$(4.9 \pm 0.1) \times 10^{5}$	$(6.6 \pm 0.2) \times 10^{-4}$	0.9804
HY6-F9	F-biotin	$(5.0 \pm 1.2) \times 10^{-11}$	$(1.4 \pm 0.01) \times 10^{5}$	$(6.8 \pm 1.6) \times 10^{-6}$	0.9999

NDB, no detectable binding.

To examine whether these mAbs demonstrate any similarity to native binding mechanisms of opioids, we compared the structure of HY4-1F9 with the human μ-opioid receptor (MOR) bound to a morphinan antagonist.[34] The MOR showed nearly no binding site similarity to HY4-1F9 or 9B1, with the morphinan ligand binding "sideways" in a solvent-accessible pocket (Figure 2C) rather than amine down. As described previously by Manglik et al.,[34] three residues coordinate the ligand, with the opioid resting within an open binding pocket. Like the HNR, the MOR binds a diverse number of structurally related ligands. MOR shows strong binding to morphine, ~2.5 nM,[35] although Manglik et al.[34] note that even the highest affinity morphinan analogs exhibit high off rates. The MOR binding mechanism favors rapid association and dissociation,[36] a notable difference from the structure and low K_{dis} shown by HY4-1F9.

Structural characterization of HY2-A12 in complex with oxycodone

Oxycodone-binding mAb HY2-A12 was isolated from mice immunized with a conjugate vaccine consisting of an oxycodone-based hapten attached at the C-6 alcohol, replacing the ketone group with a ketoxime $(Gly)_4$ linker to sKLH.[20] OXY-sKLH has been shown to be effective against heroin and its metabolites.[20,37] This conjugate vaccine is currently in phase I clinical trials in subjects with an OUD (NCT04458545). BLI indicated that HY2-A12 has an affinity of 1.0 nM for the biotinylated oxycodone hapten (Table 3 and Figure S5). We solved the structure of the HY2-A12 Fab bound to oxycodone to 2.2 Å, with three Fabs in the unit cell (Table 1). This solution is notable, as it displays 3-fold translational non-crystallographic symmetry (tNCS) within the P1 space group (see supplemental information).

The oxycodone-binding site is predominantly formed by the CDRH3. The CDRH3 wraps around the "back" of the ligand, extending along the "left" side and displacing the CDRLs, per the orientation in Figure 3. This leads to a shallow pocket with the "top" of the ligand solvent exposed (Figure 3A). Yet the CDRH2 forms multiple interactions on the "right" side of the oxycodone, pulling the ligand away from the LC and CDRH3. The tertiary amine of oxycodone (pK_a 8.8) would be ~50% protonated under crystallization conditions (pH 8.5, Table 2)[38] and protonated under physiological conditions. As with HY4-1F9, BLI showed only a slight increase in K_D at non-neutral pH (Table 4). The amine and C-14 hydroxyl group are both coordinated by the CDRH2, forming three hydrogen bonds, 2.5 Å to 2.7 Å in length, to $Glu50_{HC}$ and $Tyr52_{HC}$, respectively. Beyond this network only $Tyr33_{HC}$ and $Trp100E_{HC}$ contact the ligand, with $Tyr33_{HC}$ forming a π-cation interaction with the amine. $Trp100E_{HC}$ specifically is locked in position by the backbone of $Tyr100A_{HC}$ (Figure 3A).

Prior to our structure of HY2-A12, there were no oxycodone-binding proteins deposited in the PDB. Consequently, we compared HY4-1F9 and HY2-A12, as oxycodone differs from morphine by only the C-14 hydroxyl and C-9 methoxy groups. These antibodies share a mouse LC germline gene, IGLV1*01, which is also shared with 9B1.[33] We aligned the FV domains of HY2-A12 and HY4-1F9 (0.750 Å RMSD over 187 Cα atoms).[28] Despite this similarity, the two LC residues that assist in binding in HY4-1F9, $Tyr32_{LC}$ and $Trp91_{LC}$, do not form the same π bonds in HY2-A12 despite being conserved. With the CDRH2 pulling the ligand toward the "right," $Tyr33_{HC,\ HY2\text{-}A12}$ functionally replaces $Trp91_{LC,\ HY4\text{–}1F9}$ (Figure 3B). In the HY2-A12 HC germline IGHV1-77*01, both $Glu50_{HC}$ and $Tyr52_{HC}$ are somatically hypermutated residues, suggesting that this may be a preferred alternative binding mechanism.[33] Besides having an additional available functional group, the C-14 hydroxyl, oxycodone, has a less available group at the C-3 aromatic ring, a methoxy group. These features may be the cause of increased CDRH2 and decreased CDRH3 interaction for HY2-A12 (Figure 3C). The use of the $Trp91_{LC}$ pyrrole ring and a hydrogen bonding network, and the lack of CDRH3 interaction, are the most significant differences between HY2-A12 and HY4-1F9 and may explain their disparate affinities (Table 3).

Structural characterization of HY6-F9 in complex with fentanyl

HY6-F9 was isolated from mice immunized with a conjugate vaccine consisting of a fentanyl-based hapten attached at the terminal carbon of the two-carbon chain and replacing the aromatic ring with a glutaric amide $(Gly)_4$ linker to sKLH (Figure S1). F-sKLH has been shown to be effective against fentanyl.[20] BLI indicated that HY6-F9 has an affinity of <100 pM for the biotinylated fentanyl hapten (Table 3 and Figure S5). We solved the structure of HY6-F9 Fab bound to fentanyl to a resolution of 1.75 Å, with nine Fabs in the unit cell (Table 1). This solution

Table 4. pH-dependent binding of NIC311, HY2-A12, and HY4-1F9 by BLI

mAb ID	Antigen	pH	K_D (nM)	Error (nM)
NIC311	3AmNic-biotin	5.8	1.86	0.03
		7.4	2.4	0.04
		10.0	2.4	0.06
HY2-A12	OXY-biotin	5.8	1.66	0.043
		7.4	0.54	0.009
		10.0	0.98	0.011
HY4-1F9	MOR-biotin	5.8	<0.1	0.003
		7.4	0.10	0.003
		10.0	0.27	0.007

is notable, as there are nine tNCS-related copies within the unit cell in the $P3_1$ space group (see supplemental information).

The binding site of fentanyl in HY6-F9 is difficult to characterize, as each chain runs along each "side" of the ligand, forming a long pocket with multiple points of contact (Figure 4A), where the ligand is ~85% buried (Figure S2). Fentanyl has a pK_a of 8.99 and its protonation state is uncertain in this structure,[31] although the residues $Asn99_{HC}$, $Asn91_{LC}$, and $Trp96_{LC}$ are in position to form multiple hydrogen bonds (Figure 4B). At a physiological pH of ~7.4, these bonds are likely formed. The CDRH3 folds over the ligand and forms a hydrogen bond between the protonated tertiary amine of the piperidine ring and either the $Asn99_{HC}$ side chain or backbone (Figure 4B). In the event of the side chain contributing to this interaction, the aromatic ring of the N-phenyl group in fentanyl may also form a π-cation interaction with the partially charged side chain. The clamp-like action of fentanyl on $Asn99_{HC}$ is a key interaction, with fentanyl burying nearly 100 $Å^2$ of the residue, by far the largest single CSA observed in all mAbs (Figure 4C). This also may be the structural basis for the low K_{dis} of HY6-F9.

Opposite $Asn99_{HC}$, the $Asn91_{LC}$ side chain hydrogen bonds the ketone group of fentanyl, and that same ketone can hydrogen bond with the $Trp96_{LC}$ side chain, possibly in equilibrium with $Asn91_{LC}$ (Figure 4B). This hydrogen bond redundancy is unique among the mAb:ligand complexes investigated. The hydrogen bond between $Trp96_{LC}$ or $Asn91_{LC}$ and the fentanyl ketone forms a partial charge, allowing π-cation interaction of $Tyr95_{HC}$ with the adjacent carbon. Additionally, a π-π interaction appears to form between the phenethyl ring of fentanyl and $His27D_{LC}$ (Figure 4B). We note that this phenethyl ring is not present in the fentanyl-sKLH hapten-carrier conjugate (F-sKLH, Figure S1), and thus this bond is likely not a result of affinity maturation.

HY6-F9 has two additional binding site features beyond distinct bonds. First, a small hydrophobic pocket is formed at the base of the ligand. This shallow pocket sequesters only the ethyl group and part of the N-phenyl ring, a large hydrophobic region of the ligand (Figure 4A). As the phenethyl ring would be replaced by the F-sKLH vaccine linker, no hydrophobic pocket is observed for that group. Second, there is a hydrogen bond network between CDRL1, CDRL2, and CRDH3 (Figure 4B). These bonds are not involved in ligand binding; rather, they pull the CDRH3 toward the LC and over the fentanyl. A recent preprint[39] identified fentanyl-binding mAbs with some sequence similarity to HY6-F9. These authors note that the apo-form crystallization was not successful, an observation we also made. They attribute this to significant CDR flexibility, suggesting an induced-fit mechanism, and support this with isothermal titration calorimetry experiments.[39] With the large CSA of fentanyl to $Asn99_{HC}$, we believe that the tip of the CDRH3 loop may move into place following drug binding, an induced-fit mechanism, with the observed hydrogen bond network assisting in positioning this loop.

Prior to our structure of HY6-F9, no fentanyl:mAb structures were deposited in the PDB. Another recent study described two isolated fentanyl-binding mAbs and performed *in silico* modeling of those mAbs.[17] One sequence, P1C3H9, had 81% similarity in the HC and 95% in the LC to HY6-F9 (Figure 4C). Within the HC the hydrophobic pocket appears conserved, although significant differences are present within the CDRH3. However, the key residue for binding, $Asn99_{HC}$, is present in an adjacent location. Their model shows a highly similar Fab structure and CDR arrangement, but these authors report a differently structured binding site with no tertiary amine coordination. Taking these similarities into account, along with the shown preference for the tertiary amine motif, we believe that empirical structural determination of P1C3H9 would reveal a highly similar mode of binding to HY6-F9 as described here.

DISCUSSION

Vaccine and mAb development is a complex process: vaccine-induced polyclonal antibodies and mAbs require high affinity and specificity for the drug target, functional groups require more specific targeting owing to their relative scarcity on small ligands, and hapten linker placement must consider functional group availability and linker egress. However, despite robust work in the field of anti-opioid and anti-drug mAbs over the last 50 years, few structures of mAb against drugs of abuse, and even fewer opioid-mAb structures, have been deposited in the PDB. This limitation has significantly impacted the field's ability to rationally design new vaccines or modify existing mAbs. Our structures of four unique mAbs bound to their target drugs show that these mAbs share a protonated tertiary amine-binding motif, providing specificity, high affinity, and low off-rate for their target ligands. This amine is commonly, but not exclusively, bound by an electronegative residue, most often a germline-encoded glutamic acid in the CDRH2 of the mAb. In cases where a suitable germline residue was absent, an electronegative residue was acquired by somatic hypermutation. We observed this mode of binding in all four structures reported as well as in three of four currently published structures used for comparison.[27,32,34]

In three structures (9B1, HY2-A12, and MOR) the key electronegative residue is also part of a catemer-like motif. In MOR and HY2-A12 (Figures 2C and 3A), the second Glu residue is replaced by a Tyr or Asn, respectively. All other structures form discrete hydrogen bonds without a delocalized hydrogen bonding network. This may indicate that a hydrogen bonding network is unfavorable for small drug binding when a low off-rate is desired, as a network is more tolerant to the dissociation of a single bond. Rather, a discrete H bond is more resilient if

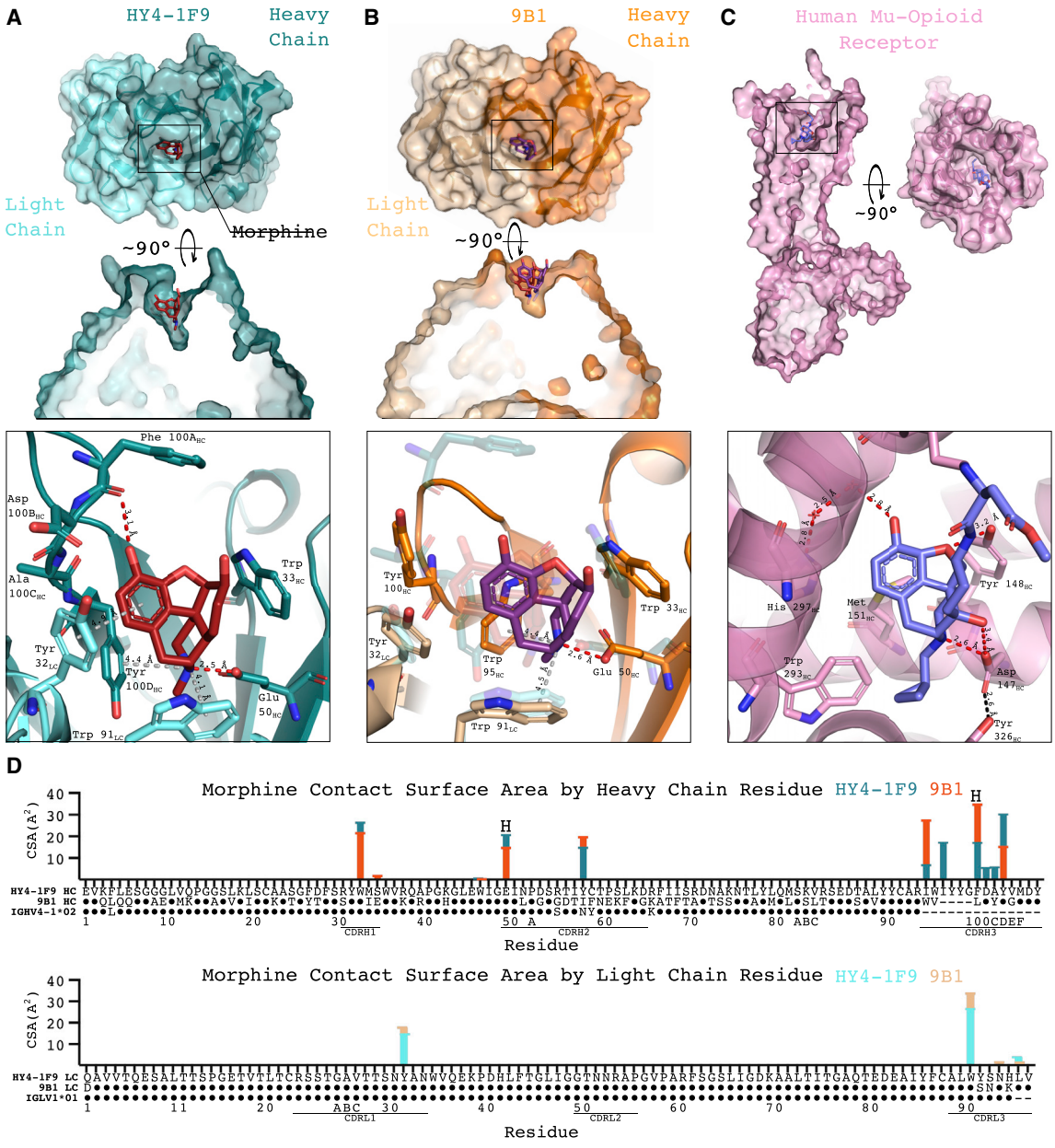

Figure 2. Structures of HY4-1F9 Fab in complex with morphine, compared with the known 9B1 Fab bound to morphine and the human μ-opioid receptor bound to a morphinan antagonist

(A) Top: surface representation of a top-down and cutaway view of HY4-1F9 with morphine shown as red sticks. Bottom: an in-depth view of the binding site, with key residues shown as sticks. Red bonds indicate hydrogen bonding and gray bonds van der Waals interactions.

(B) Top: 9B1 is shown in the same orientation as HY4-1F9 with morphine shown as purple sticks. Bottom: the binding site is shown with HY4-1F9 superimposed in transparency.

(C) Top: the human μ-opioid receptor (MOR) is shown covalently bound to a morphinan antagonist, shown as violet sticks. Bottom: the binding site is shown with key residues shown as sticks. Waters are shown as red stars, and interprotein hydrogen bonds are shown in black.

(D) CSA plot of the morphine ligand and HY4-1F9 or 9B1 residues, with a sequence alignment of HY4-1F9, 9B1 and the germline V genes shown below. Residues involved in hydrogen bonding are marked with a "H." Bar data are superimposed. Dots indicate conserved residues, dashes indicate gaps in the aligned sequences, and the numbering and CDRs are true to HY4-1F9.

electrostatic charges are only satisfied upon binding. The mAbs with the lowest K_{dis} identified, HY4-1F9 and HY6-F9, exhibit clear examples of discrete hydrogen bonding, in addition to extensive π interactions which would not be present in an aqueous solvent. The bonding networks seen in HY2-A12 (Table 3), MOR and, to a lesser extent, 9B1, do not provide the same electrostatic strength, as networks allow easier dissociation owing to their delocalized electrons. We note that while HY6-F9 does not form the same 1:1 H bonds as does HY4-1F9, $Asn99_{HC}$ is a single residue, while $Asn91_{LC}$ and $Trp96_{LC}$

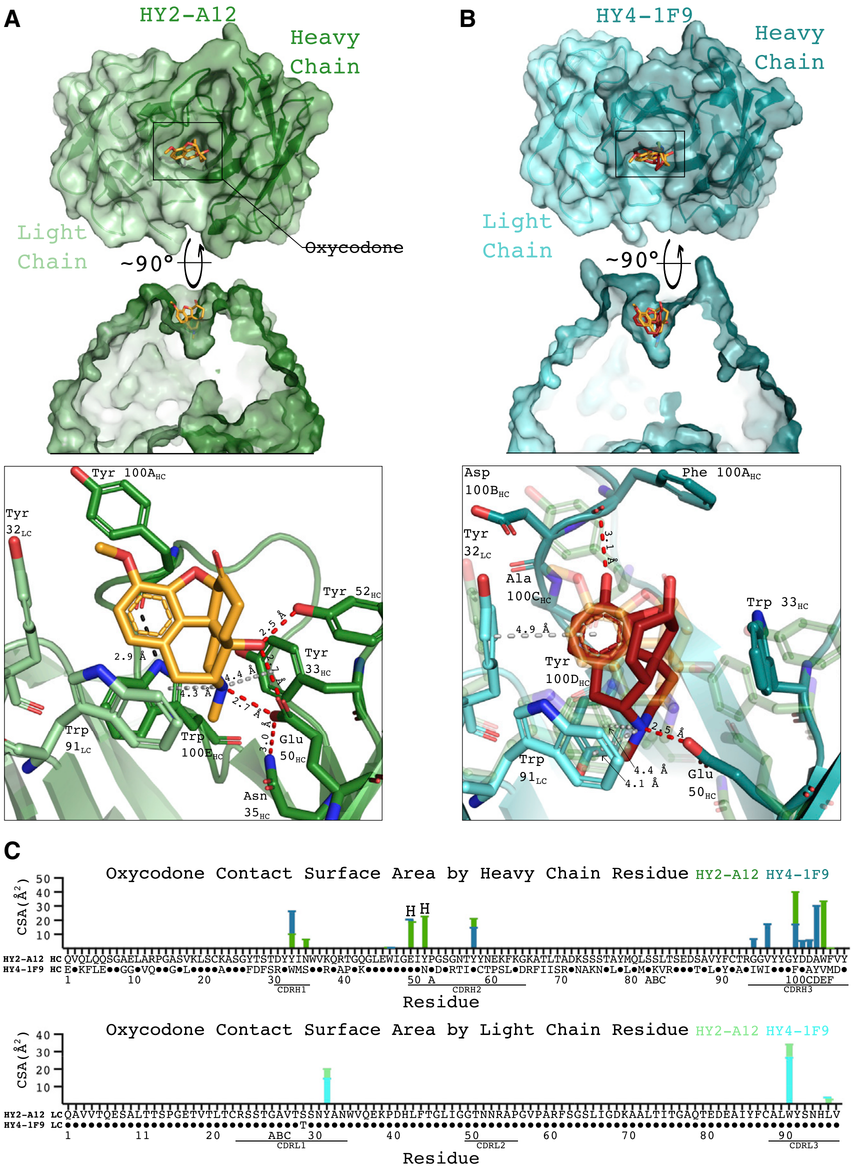

Figure 3. Structures of HY2-A12 Fab in complex with oxycodone, compared with HY4-1F9 Fab in complex with morphine

(A) Top: top and side cutaway views of HY2-A12 Fab shown in surface representation with oxycodone shown as orange sticks. Bottom: a detailed binding site view. Red bonds indicate hydrogen bonding, gray bonds indicate van der Waals interactions, and black bonds indicate intra-Fab bonds.

(B) Top: top and side cutaway views of HY4-1F9 with morphine shown as red sticks and oxycodone superimposed as orange sticks. Bottom: the binding site is shown in depth.

(C) CSA plot of the oxycodone ligand and HY2-A12 or HY4-1F9 residues, with a sequence alignment of HY2-A12 and HY4-1F9 shown below. Residues involved in hydrogen bonding are marked with an "H." Bar data are superimposed. Dots indicate conserved residues, dashes indicate gaps in the aligned sequences, and the numbering and CDRs are true to HY2-A12.

are not able to form a hydrogen bond network that would favor dissociation. This binding mode may be more suitable when the ligand has the surface area to accommodate a greater number of interacting residues (Figure S2). The need for discrete bonds may be an additional consideration when optimizing the mAb-binding site for use in prophylactic or rescue mAb treatments.

We found a distinct lack of structural homology between known drug receptors and these mAbs. These differences may be a result of the distinct attributes required of human opioid receptors and B cell receptors (BCRs) or mAbs. While high affinity is often desirable, the HNR binds diverse ligands beyond nicotine, and ligand binding is only one step in receptor structural rearrangement, a repetitive process requiring both binding and dissociation.[30] The MOR binds to a diverse drug repertoire with a high off-rate,[34,36] a feature of the large, solvent-exposed binding site. While both the HNR and MOR achieve high affinity with binding modes distinct from our reported mAbs, their distinct biological roles are not compatible with the features of high specificity and a low off-rate. To achieve all three necessary characteristics, we believe that the structural features observed in these mAbs may provide the best, though not the only, starting place: discrete functional group coordination starting with the tertiary amine, strong electrostatic complementarity, and complementary aromatic pockets to sequester hydrophobic regions.

The mAbs HY4-1F9 and HY2-A12 are unique in that they display cross-neutralizing potential for both oxycodone and morphine (Table 3) and share a LC germline (IGLV1*01). If non-cognate ligand binding is considered, HY4-1F9 binding oxycodone and HY2-A12 binding morphine, we find that HY4-1F9 still maintains 6-fold greater affinity than HY2-A12 (Table 3 and Figure S5). These complexes would only be coordinated by their tertiary amine (Figures 3A and 3B), suggesting that HY4-1F9 displays a superior amine-binding site. The replacement of Trp91$_{LC}$ by the pyrrole ring of Trp100E$_{HC,\ HY2\text{-}A12}$, and the bond network between Asn35$_{HC,HY2\text{-}A12}$, Glu50$_{HC,HY2\text{-}A12}$, and Tyr52$_{HC,HY2\text{-}A12}$, likely contribute to this inferior binding site. Notably, while the K_D is only 6-fold different, the K_{dis} of the non-cognate binding has a 10-fold difference. This suggests that while a Trp-containing site forms the cationic bond as favorably as a Tyr, the stability of this bonding system is less.

These structures provide evidence, in the form of structural features, binding modes, and specific residue preferences, for several improvements that could be made to current haptens. With the current oxycodone-sKLH hapten design (Figure S1), two oxycodone functional groups contact the mAb: the tertiary amine and C-14 hydroxyl group (Figure 3). By switching the linker position to the aromatic ring, the C-6 ketone group is free to interact with BCRs, potentially allowing for bond formation with

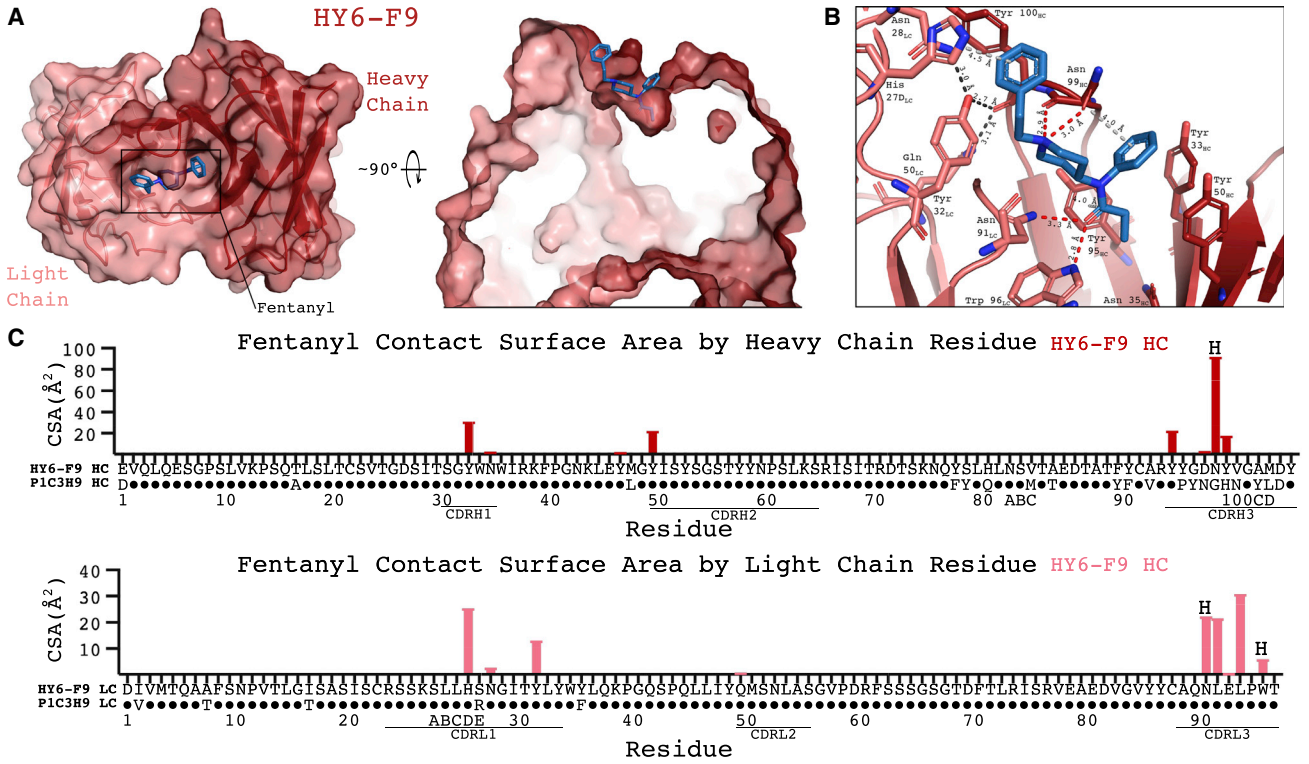

Figure 4. Structure of HY6-F9.6 Fab in complex with fentanyl

(A) Top-down and cutaway side views of surface representation of the HY6-F9.6 binding pocket, with fentanyl shown as blue sticks.

(B) The binding pocket is shown in depth. Red bonds correspond to hydrogen bonds, light-gray bonds to van der Waals interactions, and black bonds to intra-Fab hydrogen or salt-bridge bonds.

(C) CSA plot of the fentanyl ligand and HY6-F9.6 residues, with a sequence alignment of HY6-F9.6 and P1C3H9 shown below. Residues involved in hydrogen bonding are marked with an "H." Dots indicate conserved residues, dashes indicate gaps in the aligned sequence, and the numbering and CDRs are true to HY6-F9.6.

the nearby CDRH3. In the structure of HY6-F9, the mAb displays some favorable contacts with the phenethyl ring of fentanyl, specifically via His27D$_{LC}$. Yet this ring is not present in the fentanyl-sKLH vaccine, meaning that this interaction appears to be happenstance. A vaccine that includes all possible functional groups of the free drug, including relatively non-reactive groups such as phenyl rings, with consideration for which position is most accessible for linker egress, could lead to binding improvements through more complete affinity maturation. The prevalence of π-π bonding potential suggests that haptens such as F1, which removes the phenyl ring, may be suboptimal if we desire to maximize ligand-Fab contacts. Alternatively, mAb mutations could be made to take advantage of functional groups that are disrupted to allow linker conjugation. For HY4-1F9, it may be possible to engineer greater affinity to the free drug by introducing mutations to bind the C-6 hydroxyl group that is removed in the morphine-sKLH vaccine. Similar improvements could be made to HY2-A12 and HY6-F9. Further experiments of interest may include engineering stronger electrostatic complementarity by replacing H-bond-forming aliphatic residues with a structurally similar charged residue. Additionally, structurally related haptens with different linker placement have shown distinct B cell engagement and can elicit non-overlapping antibodies.[40,41] Fluorination and other chemical modifications of haptens can also translate into different vaccine efficacy against a target drug.[42] Investigating the structural basis of the ligand-mAb interaction could translate to optimizing B cell engagement through rationally designed vaccines. This understanding of the structural basis behind drug-mAb interactions is also important in Food and Drug Administration approval and bringing antibody-based products against fentanyl and its analogs to market.

Understanding ligand-protein binding poses unique challenges beyond those observed in engineering protein-protein interactions. Through examining a structurally diverse set of ligands that constitute a drug class of significant interest and analyzing shared binding attributes, we have found evidence of a preferred "starting point" and desirable structural features to acquire when considering drug binding based on available functional groups. By identifying these principles and applying them to the understanding of hapten-BCR interactions, we hope to develop optimal vaccines and more potent mAbs to treat emerging illicit drug targets.

STAR★METHODS

Detailed methods are provided in the online version of this paper and include the following:

SUPPLEMENTAL INFORMATION

Supplemental information can be found online at https://doi.org/10.1016/j.str.2022.11.008.

ACKNOWLEDGMENTS

We are particularly grateful to Julian Simon and Nick Hurlburt for their help in reviewing and preparing this paper and its figures, and to Leo Stamatatos for use of laboratory space and equipment. We are grateful to Mark LeSage for the gift of NIC311 IgG. We thank the J.B. Pendleton Charitable Trust for its generous support of Formulatrix robotic instruments. This work was funded by grants UG3 DA047711 and U01 DA051658 from the National Institutes of Health (NIH) and the National Institute on Drug Abuse (NIDA) (M. Pravetoni and M. Pancera). Some results shown in this report are derived from work performed at Argonne National Laboratory, Structural Biology Center at the Advanced Photon Source, under US Department of Energy, Office of Biological and Environmental Research contract DE-AC02-06CH11357. Further work was performed at the Berkeley Center for Structural Biology, which is supported in part by the Howard Hughes Medical Institute. The Advanced Light Source is a Department of Energy Office of Science User Facility under contract no. DE-AC02-05CH11231. The Pilatus detector on 5.0.1. was funded under NIH grant S10 OD021832. The ALS-ENABLE beamlines are supported in part by the NIH, National Institute of General Medical Sciences, grant P30 GM124169. Some molecular graphics and analyses were performed with UCSF ChimeraX, developed by the Resource for Biocomputing, Visualization, and Informatics at the University of California, San Francisco, with support from NIH R01 GM129325 and the Office of Cyber Infrastructure and Computational Biology, National Institute of Allergy and Infectious Diseases. The graphical abstract was created with BioRender.com.

AUTHOR CONTRIBUTIONS

Conceptualization, J.V.R., C.B., D.H., T.L.L., C.W., M. Pravetoni, and M. Pancera; methodology, J.V.R., C.B., D.H., T.L.L., C.W., M. Pravetoni, and M. Pancera; investigation, J.V.R., C.B., D.H., T.L.L., C.W., and A.W.; resources, C.B., D.H., R.J., S.R., and M. Pravetoni; formal analysis, J.V.R., T.L.L., C.W., and P.B.R.; writing – original draft, J.V.R and M. Pancera; writing – review and editing, J.V.R., C.B., D.H., A.T.M., R.K.S., M. Pravetoni, and M. Pancera; supervision, J.V.R., R.K.S., M. Pravetoni, and M. Pancera; funding acquisition, M. Pravetoni and M. Pancera.

DECLARATION OF INTERESTS

M. Pravetoni, D.H., and C.B. are inventors of provisional and non-provisional patent applications covering the anti-fentanyl mAbs described herein.

INCLUSION AND DIVERSITY

One or more of the authors of this paper self-identifies as an underrepresented ethnic minority in their field of research or within their geographical location. One or more of the authors of this paper self-identifies as a gender minority in their field of research. One or more of the authors of this paper self-identifies as a member of the LGBTQIA+ community. While citing references scientifically relevant for this work, we also actively worked to promote gender balance in our reference list.

Received: March 4, 2022
Revised: August 3, 2022
Accepted: November 16, 2022
Published: December 12, 2022

REFERENCES

1. Ahmad, F.B., Rossen, L.M., and Sutton, P. (2022). Provisional Drug Overdose Death Counts (National Center for Health Statistics).
2. Alexander, G.C., Stoller, K.B., Haffajee, R.L., and Saloner, B. (2020). An epidemic in the midst of a pandemic: opioid use disorder and COVID-19. Ann. Intern. Med. *173*, 57–58. https://doi.org/10.7326/M20-1141.
3. Sharma, A., Kelly, S.M., Mitchell, S.G., Gryczynski, J., O'Grady, K.E., and Schwartz, R.P. (2017). Update on barriers to pharmacotherapy for opioid use disorders. Curr. Psychiatry Rep. *19*, 35. https://doi.org/10.1007/S11920-017-0783-9.
4. Pravetoni, M., and Comer, S.D. (2019). Development of vaccines to treat opioid use disorders and reduce incidence of overdose. Neuropharmacology *158*, 107662. https://doi.org/10.1016/j.neuropharm.2019.06.001.
5. SAMHSA (2021). Key Substance Use and Mental Health Indicators in the United States: Results from the 2020 National Survey on Drug Use and Health (Center for Behavioral Health Statistics and Quality, Substance Abuse and Mental Health Services Administration).
6. UNODC (2021). World Drug Report. Sales No. E.21.XI.8 ed. United Nations.
7. Noble, F., and Marie, N. (2018). Management of opioid addiction with opioid substitution treatments: beyond methadone and buprenorphine. Front. Psychiatry *9*, 742. https://doi.org/10.3389/fpsyt.2018.00742.
8. Joudrey, P.J., Adams, Z.M., Bach, P., Van Buren, S., Chaiton, J.A., Ehrenfeld, L., Guerra, M.E., Gleeson, B., Kimmel, S.D., Medley, A., et al. (2021). Methadone access for opioid use disorder during the COVID-19 pandemic within the United States and Canada. JAMA Netw. Open *4*. e2118223. https://doi.org/10.1001/JAMANETWORKOPEN.2021.18223.
9. Elkbuli, A., Polcz, V., Dowd, B., McKenney, M., and Prado, G. (2019). Higher doses of naloxone are needed in the synthetic opiod era. Subst. Abuse Treat. Prev. Policy *14*, 1–6. https://doi.org/10.1186/S13011-019-0195-4/FIGURES/1.
10. Harvey, L., Taylor, J.L., Assoumou, S.A., Kehoe, J., Schechter-Perkins, E.M., Bernstein, E., and Walley, A.Y. (2021). Sexually transmitted and blood-borne infections among patients presenting to a low-barrier substance use disorder medication clinic. J. Addict. Med. *15*, 461–467. https://doi.org/10.1097/ADM.0000000000000801.
11. Rodda, L.N., West, K.L., and LeSaint, K.T. (2020). Opioid overdose–related emergency department visits and accidental deaths during the COVID-19 pandemic. J. Urban Health *97*, 808–813. https://doi.org/10.1007/S11524-020-00486-Y/FIGURES/3.
12. Stuart, G.L., Shorey, R.C., France, C.R., Macfie, J., Bell, K., Fortner, K.B., Towers, C.V., Schkolnik, P., and Ramsey, S. (2018). Empirical studies addressing the opioid epidemic: an urgent call for research. Subst. Abuse *12*. 1178221818784294. https://doi.org/10.1177/1178221818784294.

13. Volkow, N.D., and Collins, F.S. (2017). The role of science in addressing the opioid crisis. N. Engl. J. Med. *377*, 391–394. https://doi.org/10.1056/nejmsr1706626.

14. Smith, L.C., Bremer, P.T., Hwang, C.S., Zhou, B., Ellis, B., Hixon, M.S., and Janda, K.D. (2019). Monoclonal antibodies for combating synthetic opioid intoxication. J. Am. Chem. Soc. *141*, 10489–10503. https://doi.org/10.1021/jacs.9b04872.

15. Tenney, R.D., Blake, S., Bremer, P.T., Zhou, B., Hwang, C.S., Poklis, J.L., et al. (2019). Vaccine blunts fentanyl potency in male rhesus monkeys. Neuropharmacology *158*. https://doi.org/10.1016/j.neuropharm.2019.107730.

16. Baehr, C.A., Wu, M.M., Pandit, S.G., Arias-Umana, J., AuCoin, D., and Pravetoni, M. (2022). Pharmacological profiling of antifentanyl monoclonal antibodies in combination with naloxone in pre- and postexposure models of fentanyl toxicity. J. Pharmacol. Exp. Therapeut. *381*, 129–136. https://doi.org/10.1124/jpet.121.001048.

17. Ban, B., Barrientos, R.C., Oertel, T., Komla, E., Whalen, C., Sopko, M., You, Y., Banerjee, P., Sulima, A., Jacobson, A.E., et al. (2021). Novel chimeric monoclonal antibodies that block fentanyl effects and alter fentanyl biodistribution in mice. mAbs *13*. 1991552. https://doi.org/10.1080/19420862.2021.1991552.

18. Pentel, P.R., and LeSage, M.G. (2014). New directions in nicotine vaccine design and use. Adv. Pharmacol. *69*, 553–580. https://doi.org/10.1016/B978-0-12-420118-7.00014-7.

19. Marckel, J.A., Wetzel, H.N., Amlal, S., Amlal, H., and Norman, A.B. (2019). A recombinant humanized anticocaine monoclonal antibody alters the urinary clearance of cocaine and its metabolites in rats. Drug Metab. Dispos. *47*, 184–188. https://doi.org/10.1124/dmd.118.083857.

20. Baehr, C., Kelcher, A.H., Khaimraj, A., Reed, D.E., Pandit, S.G., AuCoin, D., Averick, S., and Pravetoni, M. (2020). Monoclonal antibodies counteract opioid-induced behavioral and toxic effects in mice and rats. J. Pharmacol. Exp. Therapeut. *375*, 469–477. https://doi.org/10.1124/JPET.120.000124.

21. Bloom, B.T., and Bushell, M.J. (2022). Vaccines against drug abuse-are we there yet? Vaccines *10*, 860. https://doi.org/10.3390/vaccines10060860.

22. Keyler, D.E., Roiko, S.A., Benlhabib, E., LeSage, M.G., St. Peter, J.V., Stewart, S., Fuller, S., Le, C.T., and Pentel, P.R. (2005). Monoclonal nicotine-specific antibodies reduce nicotine distribution to brain in rats: dose- and affinity-response relationships. Drug Metab. Dispos. *33*, 1056–1061. https://doi.org/10.1124/dmd.105.004234.

23. Williams, C.J., Headd, J.J., Moriarty, N.W., Prisant, M.G., Videau, L.L., Deis, L.N., Verma, V., Keedy, D.A., Hintze, B.J., Chen, V.B., et al. (2018). MolProbity: More and better reference data for improved all-atom structure validation. Protein Sci. 27, 293–315.

24. Wu, T.T., and Kabat, E.A. (1970). An analysis of the sequences of the variable regions of bence jones proteins and myeloma light chains and their implications for antibody complementarity. J. Exp. Med. *132*, 211–250. https://doi.org/10.1084/jem.132.2.211.

25. Ribeiro, J., Ríos-Vera, C., Melo, F., and Schüller, A. (2019). Calculation of accurate interatomic contact surface areas for the quantitative analysis of non-bonded molecular interactions. Bioinformatics *35*, 3499–3501. https://doi.org/10.1093/bioinformatics/btz062.

26. Duell, A.K., Pankow, J.F., and Peyton, D.H. (2020). Nicotine in tobacco product aerosols: 'It's déjà vu all over again'. Tob. Control *29*, 656–662. https://doi.org/10.1136/tobaccocontrol-2019-055275.

27. Tars, K., Kotelovica, S., Lipowsky, G., Bauer, M., Beerli, R.R., Bachmann, M.F., and Maurer, P. (2012). Different binding modes of free and carrier-protein-coupled nicotine in a human monoclonal antibody. J. Mol. Biol. *415*, 118–127. https://doi.org/10.1016/j.jmb.2011.10.042.

28. Schrodinger, L. (2015). The PyMOL Molecular Graphics System, Version 2.0 (Schrödinger, LLC).

29. Beerli, R.R., Bauer, M., Buser, R.B., Gwerder, M., Muntwiler, S., Maurer, P., Saudan, P., and Bachmann, M.F. (2008). Isolation of human monoclonal antibodies by mammalian cell display. Proc. Natl. Acad. Sci. USA *105*, 14336–14341. https://doi.org/10.1073/pnas.0805942105.

30. Morales-Perez, C.L., Noviello, C.M., and Hibbs, R.E. (2016). X-ray structure of the human α4β2 nicotinic receptor. Nature *538*, 411–415. https://doi.org/10.1038/NATURE19785.

31. Roy, S.D., and Flynn, G.L. (1989). Solubility behavior of narcotic analgesics in aqueous media: solubilities and dissociation constants of morphine, fentanyl, and sufentanil. Pharm. Res. *6*, 147–151. https://doi.org/10.1023/A:1015932610010.

32. Pozharski, E., Wilson, M.A., Hewagama, A., Shanafelt, A.B., Petsko, G., and Ringe, D. (2004). Anchoring a cationic ligand: the structure of the Fab fragment of the anti-morphine antibody 9B1 and its complex with morphine. J. Mol. Biol. *337*, 691–697. https://doi.org/10.1016/J.JMB.2003.12.084.

33. Ye, J., Ma, N., Madden, T.L., and Ostell, J.M. (2013). IgBLAST: an immunoglobulin variable domain sequence analysis tool. Nucleic Acids Res. *41*, W34–W40. https://doi.org/10.1093/NAR/GKT382.

34. Manglik, A., Kruse, A.C., Kobilka, T.S., Thian, F.S., Mathiesen, J.M., Sunahara, R.K., Pardo, L., Weis, W.I., Kobilka, B.K., and Granier, S. (2012). Crystal structure of the μ-opioid receptor bound to a morphinan antagonist. Nature *485*, 321–326. https://doi.org/10.1038/nature10954.

35. Crooks, P.A., Kottayil, S.G., Al-Ghananeem, A.M., Byrn, S.R., and Butterfield, D.A. (2006). Opiate receptor binding properties of morphine-dihydromorphine-and codeine 6-O-sulfate ester congeners. Bioorg. Med. Chem. Lett. *16*, 4291–4295. https://doi.org/10.1016/j.bmcl.2006.05.060.

36. Livingston, K.E., Mahoney, J.P., Manglik, A., Sunahara, R.K., and Traynor, J.R. (2018). Measuring ligand efficacy at the mu-opioid receptor using a conformational biosensor. Elife *7*. e32499. https://doi.org/10.7554/elife.32499.

37. Raleigh, M.D., Laudenbach, M., Baruffaldi, F., Peterson, S.J., Roslawski, M.J., Birnbaum, A.K., Carroll, F.I., Runyon, S.P., Winston, S., Pentel, P.R., and Pravetoni, M. (2018). Opioid dose- and route-dependent efficacy of oxycodone and heroin vaccines in rats. J. Pharmacol. Exp. Therapeut. *365*, 346–353. https://doi.org/10.1124/jpet.117.247049.

38. Mynttinen, E., Wester, N., Lilius, T., Kalso, E., Mikladal, B., Varjos, I., Sainio, S., Jiang, H., Kauppinen, E.I., Koskinen, J., and Laurila, T. (2020). Electrochemical detection of oxycodone and its main metabolites with nafion-coated single-walled carbon nanotube electrodes. Anal. Chem. *92*, 8218–8227. https://doi.org/10.1021/ACS.ANALCHEM.0C00450.

39. Triller, G., Vlachou, E.P., Hashemi, H., van Straaten, M., Zeelen, J., Kelemen, Y., et al. (2022). An epitope-focused trypanosome-derived vaccine platform elicits high-affinity antibodies and immunity against fentanyl effects. Preprint at bioRxiv. https://doi.org/10.2139/ssrn.4131714.

40. Taylor, J.J., Laudenbach, M., Tucker, A.M., Jenkins, M.K., and Pravetoni, M. (2014). Hapten-specific naive B cells are biomarkers of vaccine efficacy against drugs of abuse. J. Immunol. Methods *405*, 74–86. https://doi.org/10.1016/j.jim.2014.01.010.

41. Pravetoni, M., Keyler, D.E., Pidaparthi, R.R., Carroll, F.I., Runyon, S.P., Murtaugh, M.P., Earley, C.A., and Pentel, P.R. (2012). Structurally distinct nicotine immunogens elicit antibodies with non-overlapping specificities. Biochem. Pharmacol. *83*, 543–550. https://doi.org/10.1016/J.BCP.2011.11.004.

42. Cai, X., Tsuchikama, K., and Janda, K.D. (2013). Modulating cocaine vaccine potency through hapten fluorination. J. Am. Chem. Soc. *135*, 2971–2974. https://doi.org/10.1021/ja400356g.

43. Hicks, D., Baehr, C., Silva-Ortiz, P., Khaimraj, A., Luengas, D., Hamid, F.A., et al. (2022). Advancing humanized monoclonal antibody for counteracting fentanyl toxicity towards clinical development. Hum. Vaccin. Immunother. 2122507. https://doi.org/10.1080/21645515.2022.2122507.

44. Kabsch, W. (2010). Xds. Acta Crystallogr. D Biol. Crystallogr. *66*, 125–132. https://doi.org/10.1107/s0907444909047337.

45. Evans, P.R., and Murshudov, G.N. (2013). How good are my data and what is the resolution? Acta Crystallogr. D Biol. Crystallogr. *69*, 1204–1214. https://doi.org/10.1107/s0907444913000061.

46. Liebschner, D., Afonine, P.V., Baker, M.L., Bunkóczi, G., Chen, V.B., Croll, T.I., Hintze, B., Hung, L.-W., Jain, S., McCoy, A.J., et al. (2019). Macromolecular structure determination using X-rays, neutrons and electrons: recent developments in Phenix. Acta Crystallogr. D Struct. Biol. *75*, 861–877. https://doi.org/10.1107/s2059798319011471.

47. Pettersen, E.F., Goddard, T.D., Huang, C.C., Meng, E.C., Couch, G.S., Croll, T.I., Morris, J.H., and Ferrin, T.E. (2021). UCSF ChimeraX : structure visualization for researchers, educators, and developers. Protein Sci. *30*, 70–82. https://doi.org/10.1002/pro.3943.

48. Emsley, P., Lohkamp, B., Scott, W.G., and Cowtan, K. (2010). Features and development of Coot. Acta Crystallogr. D Biol. Crystallogr. *66*, 486–501. https://doi.org/10.1107/s0907444910007493.

49. Otwinowski, Z., and Minor, W. (1997). [20] Processing of X-Ray Diffraction Data Collected in Oscillation Mode (Elsevier), pp. 307–326. https://doi.org/10.1016/s0076-6879(97)76066-x.

50. Winn, M.D., Ballard, C.C., Cowtan, K.D., Dodson, E.J., Emsley, P., Evans, P.R., Keegan, R.M., Krissinel, E.B., Leslie, A.G.W., McCoy, A., et al. (2011). Overview of theCCP4 suite and current developments. Acta Crystallogr. D Biol. Crystallogr. *67*, 235–242. https://doi.org/10.1107/s0907444910045749.

51. Croll, T.I. (2018). ISOLDE: a physically realistic environment for model building into low-resolution electron-density maps. Acta Crystallogr. D Struct. Biol. *74*, 519–530. https://doi.org/10.1107/s2059798318002425.

STAR★METHODS

KEY RESOURCES TABLE

REAGENT or RESOURCE	SOURCE	IDENTIFIER
Antibodies		
NIC311	Dr. Mark LeSage	Keyler, D.E., et al. (2005)[22]
HY4-1F9	This Paper	N/A
HY2-A12	This Paper	N/A
HY6-F9	This Paper	N/A
Bacterial and virus strains		
NEB® 5-alpha Competent *E. coli*	New England Biolabs	Cat#: C2987H
Chemicals, peptides, and recombinant proteins		
Immobilized Ficin Resin	Thermo Scientific	Cat#: 44881
Protein A Resin	Gold Bio	Cat#: P-400-25
Protein G Resin	Gold Bio	Cat#: P-430-5
3AmNicBiotin	This paper	N/A
MOR-Biotin	Dr. Marco Pravetoni	Baehr, et al. (2020)[20]
OXY-Biotin	Dr. Marco Pravetoni	Baehr, et al. (2020)[20]
F1-Biotin	Dr. Marco Pravetoni	Baehr, et al. (2020)[20]
Critical commercial assays		
Pierce Mouse IgG1 Fab and F(ab')2 Prep Kit	Thermo Scientific	Cat#: 44980
Qiagen Plasmid Midi Kit	Qiagen	Cat#: 12145
Gibson Assembly® Master Mix	New England Biolabs	Cat#: E2611
Deposited data		
NIC311 bound to nicotine	This Paper	PDB ID # 7U61
HY4-1F9 bound to morphine	This Paper	PDB ID # 7U62
HY2-A12 bound to oxycodone	This Paper	PDB ID # 7U63
HY6-F9 bound to fentanyl	This Paper	PDB ID # 7U64
Experimental models: Cell lines		
HEK 293e cell line	ATCC	RRID:CVCL_HF20
NEB® 5-alpha Competent *E. coli*	New England Biolabs	Cat#: C2987H
Recombinant DNA		
HY6-F9 HC and LC expression vector	Dr. Marco Pravetoni	Hicks, et al. (2022)[43]
pMN Expression Vector	The Stamatatos Lab	N/A
Oligonucleotides		
Gibson Assembly: HC FWD: TCTTCCTGGTAGCGAC GGCGACTGGGGTCCATAGCGAGGTGCAGCTTCA GGAGTC	This Paper	N/A
Gibson Assembly: HC REV: AGCGAGGGGGAACACT GAGGGACCCTTAGTGCTAGCTGAGGAGACGGTGA CTGAGG	This Paper	N/A
Gibson Assembly: LC FWD: GTGCTGTTGCTCTGGG TTCCGGGATCTACTGGCGACATTGTCCTTACTCAA TCACCTGC	This Paper	N/A
Gibson Assembly: LC REV: AAGATGAACACGGAGGG TGCCGCCACCGTACGTTTGATCTCGAGCTTCGTAC CACC	This Paper	N/A
His-Fab Generation: Vector Linearization FWD: CGTCGACCAAGGGCCCATC	This Paper	N/A

(*Continued on next page*)

Continued		
REAGENT or RESOURCE	SOURCE	IDENTIFIER
His-Fab Generation: Vector Linearization REV: ACACCGGTTGCAGTTGCTACTAGA	This Paper	N/A
His-Fab Generation: Insert Amplification FWD: AACTGCAACCGGTGTACATTCCGAGGTGCAGCTTC	This Paper	N/A
His-Fab Generation: Insert Amplification REV: GCCCTTGGTCGACGCTGAGGAGACGGTGACTGAGG	This Paper	N/A
CMV Promotor Sequencing Primer: TGTCTAGAGTCCGGAG	This Paper	N/A
Software and algorithms		
XDS	Kabsch, 2010[44]	RRID:SCR_015652
AIMLESS (v. 0.7.4)	Evans and Murshudov, 2013[45]	RRID:SCR_015747
Phaser (v. 2.8.3)	Phenix	https://www.phenix-online.org/documentation/reference/phaser.html; RRID:SCR_014219
PyMOL (v 1.8.2.0)	Schrodinger, L[28]	RRID:SCR_000305
GraphPad Prism 9	GraphPad Software	RRID:SCR_002798
Phenix (v. 1.19.2-4158)	Liebschner et al., 2019[46]	http://www.phenix-online.org/
Dr_sasa	Ribeiro, et al., 2019[25]	http://schuellerlab.org/dr_sasa/download
ChimeraX (v. 1.2.5)	Pettersen, et al., 2021[47]	RRID:SCR_015872
Coot (v 0.9.6)	Emsley et al., 2010[48]	RRID:SCR_014222
HKL-2000	Otwinowski and Minor, 1997[49]	RRID:SCR_015547
Octet Analysis Software (v 12.0.2.3)	FortéBio	https://www.sartorius.com/en/products/protein-analysis/octet-bli-detection/octet-systems-software
Other		
Octet Red96e BLI System	Sartorius	Cat#: OCTETRED96E
Platinum™ SuperFi II PCR Master Mix	Thermo Fisher Scientific	Cat#: 12368010
Infusion HD Cloning Plus kit	Takara Bio	Cat#: 638920
HiLoad 16/600 Superdex 200 pg	Cytiva	Cat#: 28989335
Akta Pure System	GE Biosciences	Cat#: 29018224
MRC 2 Well Crystallization Plate in UVXPO	Swissci	Cat#: HR3-107
EasyXtal 15-Well Tool X-Seal	Nextal Biotech	Cat#: 132008
Parabar 10312	Hampton Research	Cat#: HR2-643
Expi293 Expression System	ThermFisher Scientific	Cat#: A14635
ÄKTA pure system	Cytiva	Cat#: AKTApure
HiTrap MabSelect PrismA	Cytiva	Cat#: 17549851
Streptavidin BLI Biosensors	Sartorius	Cat#: 18-5020

RESOURCE AVAILABILITY

Lead contact

Further information and requests for resources and reagents can be directed to and will be addressed by the lead contact Marie Pancera (mpancera@fredhutch.org).

Materials availability

This study generated a biotinylated nicotine hapten not previously described. Please refer to supplemental methods for synthesis information. Plasmids for expression of reported antibodies are available upon request to the lead contact. Haptens, either biotinylated or sKLH conjugated, are available upon request; please direct inquiries to Marie Pancera. All materials are subject to MTA agreements and IP restrictions where applicable.

Data and code availability

- All crystallographic datasets have been deposited in the Protein Data Bank and are publicly available as of the date of publication. Accession numbers are listed as follows: NIC311 (PDB ID 7U61), HY4-1F9 (PDB ID 7U62), HY2-A12 (PDB ID 7U63), HY6-F9 (PDB ID 7U64).

- This paper does not report original code or other original data.
- Any additional information required to reanalyze the data reported in this paper is available from the lead contact upon request.

EXPERIMENTAL MODEL AND SUBJECT DETAILS

Expression of NIC311, HY2-A12, and HY4-1F9 from murine hybridomas

Purified NIC311 IgG was a gift from Dr. Mark LeSage. HY2-A12 and HY4-1F9 monoclonal antibodies were generated from previously isolated hybridomas.[20] These hybridomas were adapted to DMEM (Corning Inc, Corning, NY) and supplemented with 10% fetal bovine serum, hypoxanthine/thymidine (Sigma), and 2-mercaptoethanol and grown in Integra Celline 1000 bioreactors (Wheaton, Millville, NJ) at 37°C, 5% CO_2. Secreted mAb was purified from cell culture supernatant by Protein A affinity chromatography using Protein A Sepharose (GE Healthcare, Chicago, IL). The purified antibody was sterilized using 0.2 mm filtration, aliquoted in preservative-free PBS, pH 7.4, and stored at 4°C.

Expression of HY6-F9 mAb

HY6-F9 mAb was produced via transient expression with the Expi293 expression system (ThermoFisher Catalog # A14635). Cells were cultured using manufacturer specified reagents and environmental conditions. Transfections were performed using a 2.5:1 ratio of LC vector:HC vector, with 1μg of total vector DNA/mL of culture volume. Cell culture supernatant was harvested 7 days following transfection.

Expression of HY6-F9 His-Fab

HY6-F9 His-Fab was expressed in HEK293e cells (RRID: CVCL_HF20). Cell transfection used 2 mL sterile PEI with 250 μg each HY6-F9 heavy chain and light chain on a pMN plasmid and 38mL sterile PBS per one liter of cells at 1 million cells/mL. Cultures were maintained in suspension and incubated at 37°C, 5% CO_2 for 6 days with shaking at 140 rpm.

METHOD DETAILS

*3*AmNic-biotin synthesis

Full Chemical Name: *N*^{1}-((1-methyl-2-(pyridin-3-yl)pyrrolidin-3-yl)methyl)-*N*^{4}-(4-(5-(2-oxohexahydro-1*H*-thieno[3,4-*d*]imidazol-4-yl) pentanamido)butyl)succinimide.

Please see Figure S6 for the reaction scheme. To a solution of carboxylate **1** (0.30 g, 1.01 mmol) in DMF (5 mL), BOP (0.67 g, 1.52 mmol) was added at room temperature, followed by the addition of a solution of TEA (0.71 mL, 5.06 mmol) and *N*-(4-aminobutyl)-5-(2-oxohexahydro-1*H*-thieno[3,4-d]imidazol-4-yl)pentanamide hydrochloride (0.44 g, 1.27 mmol) in DMF (5 mL). The reaction was stirred at room temperature for 24 h. The solvent was removed under nitrogen flow and the residue was subjected to chromatography on silica gel using 0–100% CMA80 in DCM to furnish amide **2** (133.1 mg, 22%) as a white solid. ^{1}H NMR (300 MHz, CD_3OD) δ 8.52 (s, 1H), 8.47 (d, *J* = 4.8 Hz, 1H), 7.87 (d, *J* = 7.9 Hz, 1H), 7.44 (dd, *J* = 7.8, 5.0 Hz, 1H), 4.49 (dd, *J* = 7.6, 4.9 Hz, 1H), 4.30 (dd, *J* = 7.8, 4.4 Hz, 1H), 3.28–3.33 (m, 1H), 3.22–3.14 (m, 7H), 2.97–2.87 (m, 2H), 2.70 (d, *J* = 12.7 Hz, 1H), 2.49–2.06 (m, 12H), 1.81–1.24 (m, 11H); ^{13}C NMR (75 MHz, CD_3OD) δ 176.0, 174.6, 174.4, 166.1, 150.4, 149.5, 139.1, 138.0, 125.4, 74.3, 63.4, 61.6, 57.0, 56.8, 48.7, 42.7, 41.1, 40.5, 40.1, 40.0, 36.8, 32.1,32.1, 29.8, 29.5, 28.2, 27.8, 27.8, 26.9; MS (ESI) *m/z*: calcd for $C_{29}H_{45}N_7O_4S$ 587.78, found 588.4 $[M + H]^+$; HPLC (280 nm) t_R = 8.21 min.

BLI analysis

Biolayer interferometry measurements of purified HY2-A12, HY4-1F9, HY6-F9, and NIC311 mAb were performed on an Octet Red96e system (Sartorius). Streptavidin biosensors were loaded with biotinylated haptens of oxycodone (OXY-biotin), morphine (MOR-biotin), fentanyl (F1-biotin), or nicotine (3AminoNic-biotin) at 0.1–0.2 ug/mL in PBS-T for 60 s (Baehr et al., 2020). Following a 60 s baseline measurement in PBS-T, association rate was measured with purified mAb, 5–40 nM for 3–5 min, and then dissociation rate was measured in PBS-T for 5–10 min. For analysis at non-neutral pH, following the 60 s baseline measurement in PBS-T, hapten loaded biosensors were equilibrated in 0.1 M MES +0.05% Tween 20, pH 5.8, 0.1 M carbonate-bicarbonate + 0.05% Tween 20, pH 10.0, or PBS-T buffer adjusted to a pH range of 5.0–10.0 (for the 3AmNic-biotin hapten) for 10 min prior to the association step. Dissociation constant was calculated as koff/kon by Octet analysis software (Sartorius).

Generation of HY6-F9 mAb expression vectors

Fentanyl-binding mAb VH and VL sequences were cloned into pcDNA3.4 mammalian expression vectors prepared by Genscript as described.[43] Briefly, VH and VL sequences were PCR-amplified with primers to introduce 30 bp overlap with the pcDNA3.4 vector, and inserts were introduced with Gibson Assembly® Master Mix (New England Biolabs Catalog #E2611). Cloning primers used are reported in the key resources table. Correct insertion of VH and VL was confirmed by Sanger sequencing using a primer targeting the CMV promotor.

Generation of HY6-F9 VH His-Fab expression vector

The VH region of HY6-F9 was PCR amplified from pcDNA™3.4 plasmid DNA, and a pMN destination backbone was linearized using Platinum™ SuperFi II PCR Master Mix. The VH region was cloned into the linearized pMN backbone containing a generic human CH1 region with a C-term 6xHis-tag, and an N-term secretion tag, using the Infusion HD Cloning Plus kit (Takara Bio). Primers used are available in the key resources table. The HY6-F9 chimeric His-Fab expression vector was transformed into NEB5α *E. coli* cells (New England BioLabs) and DNA was isolated using a MidiPrep (Qiagen). Expression vector sequencing was performed by Genewiz (Genewiz Inc, Seattle, WA).

Fab digestion and preparation

NIC311 and HY2-A12 – Purified NIC311 IgG_1 and HY2-A12 IgG_{2a}, each at 10 mg/mL in a 1 mL aliquot, were prepared as described in the Experimental Models section. Aliquots were individually digested using Thermo Scientific Pierce Mouse IgG1 Fab and F(ab')2 Preparation Kit (Fisher Scientific) Digested mAb was then incubated with Protein A resin (GoldBio) and the flowthrough collected.

HY4-1F9 – Monoclonal antibody was received as purified mouse IgG_1 at 10 mg/mL in a 1 mL aliquot, prepared as described in the Experimental Models section. Thermo Scientific Pierce Mouse IgG1 Fab and F(ab')2 Preparation Kit (Fisher Scientific) was used for digestion, 400uL resin slurry per 2.5mg mouse IgG1, following manufacturers protocol. Digest was allowed to run 18 h at 37°C, and digested mAb was incubated with 500 μL protein A resin (GoldBio) for 1 h at 37°C. Flowthrough was pooled and incubated with 200 μL protein G (GoldBio) with 500ul protein G binding buffer for 1 h at 23°C. Flowthrough was then collected.

HY6-F9 – HY6-F9 His-Fab was expressed in HEK293e cells as described in the Experimental Models section. The supernatant was harvested through centrifugation at 4000 × g for 20 min. The supernatant was then sterile filtered using a 0.2 μm bottle-top filter, batch bound to 4 mL Ni-NTA resin for 1 h at 23°C with shaking at 120 rpm, and then HY6-F9 Fab was eluted with 5mM Tris buffer containing 300 mM imidazole.

HY6-F9 mAb for BLI purification

mAb was purified from filtered cell culture supernatant via liquid chromatography on an ÄKTA pure (Cytiva) with a HiTrap MabSelect PrismA protein A column (Cytiva Product # 17549851) (running buffer PBS, pH 7.4, elution buffer 0.1 M Na-Acetate, pH 3.5). Eluted mAb was neutralized by dilution with 1/3rd final volume 2.5 M Tris, pH 7.2, and buffer exchanged into PBS, pH 7.4. Purified mAb concentration was determined by absorbance at 280 nm on a Nanodrop (ThermoFisher). Confirmatory analysis of purified mAb was performed by SDS-PAGE under reducing and non-reducing conditions.

SEC purification and concentration of Fabs for crystallization

Following affinity column purification, all Fabs were concentrated to 2 mL using 10 kDa Amicon® (Millipore Sigma) and sterile filtered (Ultra-Free-CL, Millipore Sigma), before injection onto a Superdex 200 16/600 size exclusion column (Cytivia) equilibrated with HEPES (5mM HEPES, 150mM NaCl, pH 7.5) buffer using an AKTApure (GE Biosciences) system. Fab peak fraction was pooled and concentrated to the listed concentration (Table 2) for crystallization trials.

Crystallization and structure determination

Fabs were incubated for >2 h at 23°C with 2-fold molar excess of their target ligand before being used for crystallization trials. NIC311 received a 3-fold molar excess of nicotine. Swissci® MRC 2 Well UVXPO plates were used to screen conditions from commercial 96-well screens using an NT8 drop setter (Formulatrix). Screens used include MCSG1-3 (Microlytic), WPS2 (Rigaku), Xtal High Throughput and Additive Screen (Hampton Research). Crystallizing conditions were optimized in EASYXTAL® 15-well crystallization trays (NextalBiotech). Final conditions that provided a diffracting crystal are shown in Table 2. Crystals were flash cooled in their crystallizing condition buffered with 30% ethylene glycol (NIC311, HY4-1F9), without cryo-protectant due to high salt content (HY6-F9), or in Paratone (Hampton Research) (HY2-A12). Data were collected at either Sector 19 of the Advanced Photon Source (Argonne National Labs), or Beamline 5.0.1 at the Advanced Light Source (Lawrence Berkeley National Lab). Beamline data were processed using XDS[44] or HKL-2000,[49] data were reduced as necessary using CCP4,[45,50] and the structures were phased and solved using the Phenix software suite,[46] the *Coot* toolkit,[48] and ChimeraX[47] with the ISOLDE plug-in.[51] Structure visualization, comparisons, and molecular representations were created in PyMol.[28] BSA and CSA calculations were performed in dr_sasa.[25] Protein interaction data were analyzed using GraphPad Prism (version 9.0.1 for Mac). All collection and refinement data are available in Table 1.

tNCS processing details

HY2-A12 - To ensure that space group assignment was correct, a self-rotation function was performed. No peaks were observed that would suggest a higher symmetry space group. X-triage corroborates the observed Fab distribution in the Patterson Peak analysis. Final refinement of the structure did not include NCS restraints. No differences are observed between tNCS related molecules.

HY6-F9.6 - Data reduction of a high-symmetry, high-tNCS crystal was complicated, with automatic data processing in XDS failing to find a suitable solution. Consequently, exhaustive data reduction in HKL-2000 in all P3 space groups was performed, with only one reasonable output found. X-triage reported tNCS fraction coordinates (0.333, −0.333, 0) and a vector length (125.943 Å) equivalent to observed Fab distribution in the solved structure. Due to the high resolution of the data, NCS restraints were not used in refinement. Two deviations between tNCS copies are noted. One Fab is rotated compared to its tNCS counterparts, although it is in a large solvent channel when symmetry mates are generated, potentially allowing this freedom of movement. Matthew's coefficient analysis

suggests 10 Fabs in the unit cell, which is incompatible with the space group and tNCS, but supports the presence of 9 Fabs with the observed large solvent channel. Alignment shows no significant variations between all Fab copies, except for minor loop motion. The second deviation is that in several copies, there is some motion of the exposed and relatively uncoordinated phenyl group of fentanyl, however no further conformation changes to the remainder of the ligand are noted.

QUANTIFICATION AND STATISTICAL ANALYSIS

All X-ray data collection and refinement statistics are shown in Table 1.